

Surface-Induced Layering of Quenched 3D Dusty Plasma Liquids: Micromotion and Structural Rearrangement

Wen Wang^{1,2}, Hao-Wei Hu,¹ and Lin I¹

¹*Department of Physics and Center for Complex Systems, National Central University, Zhongli, Taiwan 32001, Republic of China*

²*Molecular Sciences and Technology, Taiwan International Graduate Program, Academia Sinica and National Central University, Taiwan 10617, Republic of China*



(Received 28 July 2019; accepted 9 March 2020; published 22 April 2020)

We experimentally demonstrate confinement surface induced layering with a fluctuating layering front, and investigate the heterogeneous 3D crystalline ordered structure, cooperative micromotion, and structural rearrangement in the layered region of a quenched dusty plasma liquid. It is found that, after quenching the liquid with 2 to 3 layers adjacent to its flat bottom boundary, the layering front invades upward and exhibits turbulentlike fluctuations with power law decays in spatial and temporal power spectra. The layered region can be viewed as a $2 + 1D$ system with vertically coupled horizontal 2D layers, in which particle translational motions are nearly fully suppressed. Each layer exhibits hexatic structure with a slow decay of long-range triangular lattice order. The nearly parallel but with different horizontal shifts of intralayer lattice lines of adjacent layers allows the heterogeneous fcc, bcc, and hcp structures with specific lattice orientations. In each layer, particles exhibit thermally excited horizontal motions of alternative cage rattling and cooperative hopping, which cause intralayer lattice line wiggling and triangular crystalline domain rupture or healing, respectively. The different intralayer cooperative motion of adjacent layers is the key for interlayer slip causing the structural rearrangement of 3D crystalline ordered domains.

DOI: 10.1103/PhysRevLett.124.165001

Microscopically, the structure and motion of liquids without external driving are determined by three important factors: stochastic thermal agitation, mutual interaction, and topological constraint from the boundary. The latter two generate spatiotemporal ordering which can be deteriorated by the former. For example, cooling the liquid closer to the freezing point increases the ratio of mutual interaction to thermal agitation. It causes the emergence of crystalline ordered domains (CODs) with various sizes and lattice orientations, which can be rearranged through avalanchelike cooperative particle hopping [1–11]. The topological constraint of the flat boundary lines up particles and suppresses transverse motion. It leads to the formation of layered structure nearby the boundary up to the thickness about the structural correlation length of the bulk liquid [12–22]. It is also the main cause for the dynamical slowing down of the liquid in the mesoscopic gap about a few interparticle distance in width [15–22].

The recent studies on the supercooled metallic glass [23], crystallizing colloids [24–26], and quenched dusty plasmas [27] also demonstrated that further cooling the 3D liquid below the freezing point can extend the number of layers adjacent to the boundary or throughout the entire system. CODs with different 3D structures, such as bcc, fcc, and hcp with specific lattice orientations normal to the flat boundary, were also identified in the layered region of quenched colloidal systems [24–26] and 3D dusty plasma

crystals [27] with flat boundaries. Nevertheless, the intralayer structure and micromotion, and their correlation with the associated structural rearrangement (SR) of 3D COD structures, in the layered region of the quenched 3D liquid remain elusive.

For the quenched 3D cold liquid under confinement, the layered region nearby the flat boundary can be viewed as a $2 + 1D$ system composed of a stack of coupled 2D layers, in which vertical (interlayer) particle motion is strongly suppressed by the confinement effect. Recent experimental and numerical studies on Yukawa liquids without confinement effect demonstrated that the 2D cold liquid around freezing can be viewed as a patchwork of CODs with triangular lattice structure and different lattice orientations, which can be rearranged through rupture, corotation, or healing of CODs by thermally induced cooperative hopping [2,9,10].

Nevertheless, compared to the 2D cold system, the thermally excited intralayer cooperative motion is further complicated by the interlayer coupling under various local 3D microstructures in the above $2 + 1D$ system. The relative intralayer motions between adjacent layers further provide feedback to determine local 3D structures and their evolution. Moreover, the interface between the layered and the unlayered regions might not be flat, under the competition of thermal agitation and local particle interaction with various microstructures.

Therefore, it is intriguing to unravel the following unexplored important issues: (i) How does the layering front evolve spatiotemporally? (ii) What is the basic intralayer 2D structure in the layered region and how does the local relative intralayer structures of adjacent layers affect the local 3D COD structures? (iii) What are the basic thermally excited intra- and interlayer cooperative motions, and how do they affect 3D COD SR? In this work, the above issues are experimentally investigated through direct visualization at the kinetic level, using the quenched 3D dusty plasma liquid suspended above a flat sheath boundary as a platform.

The dusty plasma liquid can be formed by micrometer sized dust particles suspended in the low pressure rf discharge, through the screened Coulomb interaction due to the large negative charges ($\sim 10^3 e/\text{dust}$) on dust particles. It is a good platform to understand the generic behaviors of the Yukawa liquid at the microscopic level through direct optical tracking of individual dust particles. The past studies on the microstructure and -motion of dusty plasma liquids have been mainly focused on the 2D liquids [2,9,10,19,21,28–37], and the crystallization after quenching the 3D liquids [27,38–41].

The experiment is conducted in a cylindrical symmetric rf dusty plasma system similar to what is described elsewhere [9]. A rectangular trap 32 mm in length and 24 mm in width, in which the dusty plasma liquid formed by SiO_2 particles (1.93 μm in diameter) is confined by the sheath field adjacent to the trap wall [42]. The mean interparticle distance a in the horizontal plane is about 0.16 mm. The weakly ionized glow discharge ($n_e \sim 10^9 \text{ cm}^{-3}$) is

generated in 250 mTorr Ar gas using a 14-MHz rf power system. The estimated Debye length and dust charges are on the order of $10^2 \mu\text{m}$ and $10^3 e/\text{dust}$, respectively. The sudden change of rf power from 1 to 3 watts in 1 ms quenches the liquid and induces layering formation starting from about two layers nearby the flat bottom surface of the dust cluster suspended above the bottom sheath. The waiting time $t_w = 0 \text{ s}$ is set at the quenching time. Similarly to the previous experiment [28,42,43], a thin horizontal laser sheet 0.2 mm in thickness can be vertically scanned to obtain the top view images of three adjacent horizontal layers each with 15 Hz frame rate. Illuminated by another fixed thin vertical laser sheet, horizontally through the dust cluster center, the side view image can also be obtained. Particle positions can be digitally tracked from the CCD (charge coupled device) images.

Figure 1(a) shows the sequential snapshots of the side view images at three typical t_w s, with 0.2 s exposure time and 4 a half-width of the illuminating vertical laser sheet. Figure 1(b) shows the temporal evolution of z_f , the layering front height from the bottom first layer. Figure 1(c) shows the temporal evolution of the spatially averaged front height $\langle z_f \rangle_x$. Initially, layering with a fluctuating front [blue lines in Fig. 1(a)] only occurs in the bottom few layers. $\langle z_f \rangle_x$ grows exponentially (with exponent = 0.02 s^{-1}) in the first 75 s, and then fluctuates around a saturated level after 80 s. Figure 1(d) shows the typical power spectra S_k and S_f of the spatial and temporal evolutions of z_f after saturation, respectively. Their scale free power law decays manifest that the spatiotemporal fluctuations of the layering front follow similar dynamical laws over a broad range of

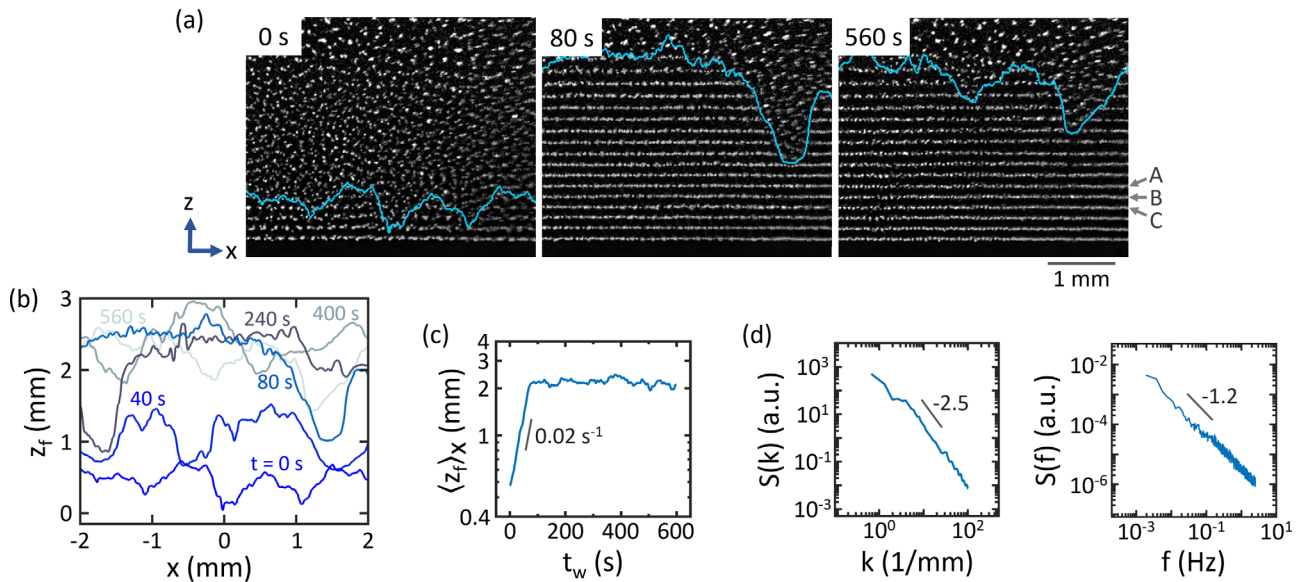


FIG. 1. (a) Sequential snapshots of the side view images at three typical t_w s, illuminated by a vertical laser sheet with 4 a half width. The blue lines indicate the layering fronts. (b) Fluctuating layering front height, z_f at several different t_w , showing the spatiotemporal evolution of the layering front. (c) Temporal evolution of the spatially averaged front height $\langle z_f \rangle_x$. (d) Power spectra S_k and S_f of the spatial and temporal evolutions of z_f for $t_w > 80 \text{ s}$. The numbers by the gray lines are the corresponding scaling exponents.

spatiotemporal scales (see Fig. S2 of the Supplemental Material for more details [42,44,45]).

Now, let us focus on the microstructure in the layered region after saturation, using that in three sequential layers *A* to *C* with descending height [see Fig. 1(a)] as an example. The left column of Fig. 2(a) shows the sequential top view snapshots of the microstructure of layer *B*, color coded by $|\Psi_6|$, where triangles and squares represent fivefold and sevenfold disclination defects, respectively. Ψ_6 is the intralayer local bond orientational order [47,48]. In each layer, the structure shows long-range triangular lattice orientation order with a small fraction of dislocation defects, which causes the weak power law decay of $g_6(r)$, the radial intralayer pair correlation function of Ψ_6 in Fig. 2(b). Locally, the intralayer structure can be rearranged, as supported by the changes of defect positions and the red patterns at different times in the left column of Fig. 2(a) and the decay of $g_6(\tau)$ (the temporal correlation function of Ψ_6) with decay time about 10 s in Fig. 2(b).

The right column of Fig. 2(a) further shows the top view particle configurations at three different t_w s, color coded by their local 3D microstructure (green, yellow, and red represent fcc, hcp, and bcc structures, respectively), in which particles of layers *A*, *B*, and *C* are sitting at the

vertices of the brown, gray, and blue grids, respectively. The method to determine 3D microstructure can be found in Supplemental Material [42]. The three adjacent layers have very similar averaged orientations of the intralayer triangular lattice and decay rates of $g_6(\tau)$ and $g_6(r)$ shown in Fig. 2(b). Note that the purple line in the left panel of Fig. 2(b) shows the $g_6(\tau)$ of $\langle\Psi_6\rangle$ (averaged over all the sites of the three layers). It reflects that spatially averaged intralayer triangular lattice orientation and structural ordering can be sustained over a long time, regardless of the local intralayer SR with local relaxation time about 10 s.

Three-dimensionally, bcc, fcc, and hcp are the three dominant structures for the CODs typically about a few a in size, which can be rearranged with increasing time. The cartoons in Fig. 2(c) showing the top views and 3D view (with the blue-gray surface corresponding to the center layer *B*) of the particle positions for the above three structures, clearly explain why bcc, hcp, and fcc structures with specific lattice orientations [110], [001], and [111] along z axis, respectively, can only be allowed. Their particles in each layer all show triangular latticelike packing, but with different relative horizontal shifts of intralayer (2D) lattice lines of adjacent layers. Namely, only those 3D structures with specific orientations can

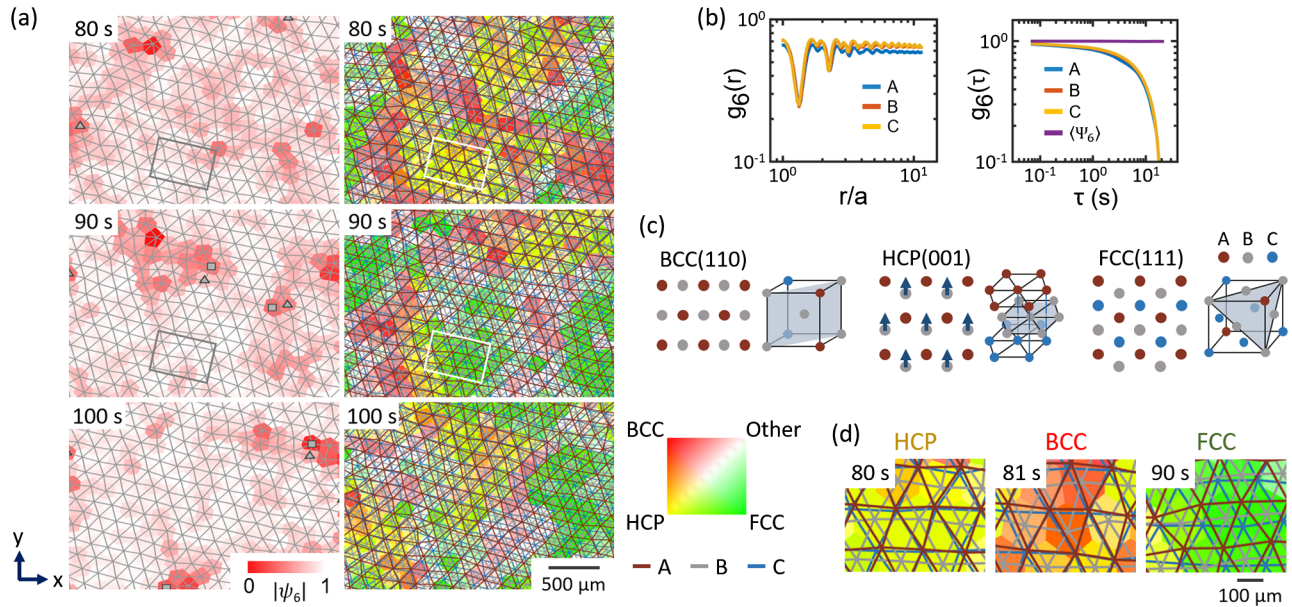


FIG. 2. (a) Left column: sequential snapshots of the microstructure of layer *B*, color coded by $|\Psi_6|$, where triangles and squares represent fivefold and sevenfold disclination defects, respectively. Right column: particle configurations at three different t_w s, color coded by their local 3D microstructure (green, yellow, and red represent fcc, hcp, and bcc structures, respectively), in which particles of layers *A*, *B*, and *C* are sitting at the vertices of the brown, gray, and blue grids, respectively. (b) Spatial and temporal pair correlation functions $g_6(r)$ and $g_6(\tau)$ of Ψ_6 in each of the three adjacent layers. Note that the purple line in the left panel is the $g_6(\tau)$ of $\langle\Psi_6\rangle$ (the spatially averaged Ψ_6 over all the sites of layers *A*, *B*, and *C*). (c) Cartoons showing the top view and 3D view (with the blue-gray surface corresponding to the middle layer) of the particle positions for the bcc, hcp, and fcc structures with specific lattice orientations, [110], [001], and [111] along the z axis, respectively. The brown, gray, and blue dots represent particles in layers *A*, *B*, and *C*, respectively. In bcc and hcp structures, brown and blue particles overlap in top view plots. The displacement of particles in layer *B* indicated by the vectors in the hcp structure can cause the change to bcc structure. (d) Enlarged plots of three layer particle configurations from the rectangular regions in (a), at 80, 81, and 90 s. The slight interlayer slip causes the changes among bcc, fcc, and hcp structures.

accommodate the similar intralayer structures with very similar long range triangular lattice orientations for adjacent layers. As illustrated by Fig. 2(c), the slight sliding of the center layer *B* along the arrow direction of the middle panel causes the change from hcp to bcc structures. The sequential enlarged plots [Fig. 2(d)] from the rectangular region of Fig. 2(a), further manifest the slight interlayer slip leads to local 3D structural evolution.

After reaching the steady state, particle motions of layered regions are not frozen but constrained in layers (the ratio of the probability of interlayer hopping to that of intralayer hopping is less than 1%) [42]. What are the generic behaviors of intralayer cooperative particle motions leading to interlayer slip and the above 3D SR? Using the plotting method of Refs. [10,29], Fig. 3(a) shows the intralayer particle trajectories color coded by displacements (top row) over 10 s starting from two typical different times, and the corresponding color coded plots of bond angle variation $\delta\theta$ of adjacent intralayer particle pairs (bottom row), over 10 s interval, for layers *A* and *B*. The background grid indicates initial particle configurations for each layer. Obviously, particles exhibit heterogeneous intralayer cooperative motions (ICMs), which can be roughly classified into small amplitude cage rattling (black trajectories) and large amplitude cooperative hopping (red trajectories in the form of drifting or rotating patches) alternatively occurring at different places. The former causes the horizontal wiggling of intralayer lattice lines in regions with alternating light green and yellow strips indicating small $|\delta\theta|$ in the lower row of Fig. 3(a). The strong relative intralayer domain drift or rotation [e.g., the circled regions in Fig. 3(a)] induces strong shear strips with large $|\delta\theta|$

indicated by the dark green (brown) strips along the boundaries of yellow (green) domains.

The intralayer motions for the two adjacent layers in Fig. 3(a) evidence that particles in different layers exhibit different ICMs. For example, the strong shear strips occur at different locations (also see Fig. S3 of Ref. [42] with a larger view). Figure 3(b) shows the two sequential plots of particle configurations of the rectangular region in Fig. 3(a) for layer *A* (dark gray grid) and layer *B* (light gray grid). The bond breaking and reconnection along the strong shear strip can be demonstrated by the strong kinks of lattice lines *A1* and *A2* (*B3* and *B4*) in layer *A* (*B*). However, the small amplitude ICM in the same region of layer *B* (*A*) only causes undulation of neighboring lattice lines *B1* and *B2* (*A3* and *A4*) without bond break or reconnection.

Namely, the strong ICM causes intralayer slipping through bond breaking and reconnection along the shear strip. The difference of ICMs of adjacent layers is the key inducing interlayer slip, which in turn causes local SR among bcc, fcc, and hcp structures as demonstrated in Fig. 2(c). Note that, comparing with the previous finding in the 2D cold dusty plasma liquid in which shear strips form a fractal structure [10,29], our shear strips have much lower number density and cannot propagate over long distance. The strong interlayer coupling dissipates thermally induced hopping energy and terminates strong shear strips propagation. It is also the cause for locking the long-range triangular lattice orientations over different layers and longtime even after many SRs.

Note that in the dusty plasma, the downward ion flow focusing behind each suspended particle could make the particle interaction anisotropic and prevent the formation of

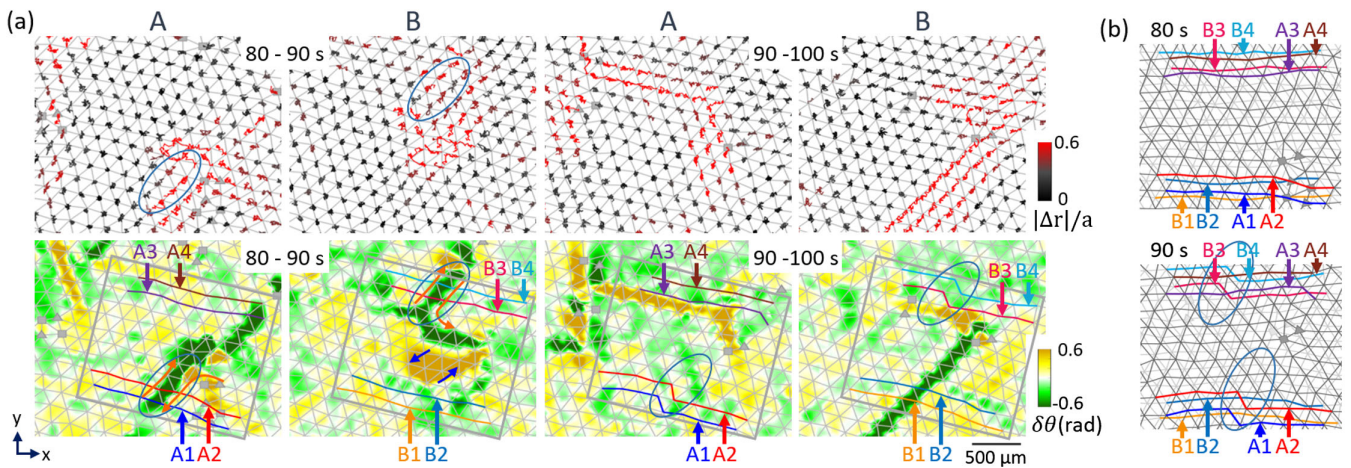


FIG. 3. (a) Top row: intralayer particle trajectories, color coded by displacements over 10 s of layers *A* and *B* starting from $t_w = 80$ and 90 s from the same region as Fig. 2(a). Bottom row: color coded plots of $\delta\theta$, the variation of the bond angle of an adjacent particle pair. The background grids indicate initial particle configurations at each t_w . (b) Two sequential plots of overlapped particle configurations in the rectangular region in (a) for layer *A* (dark gray grid) and layer *B* (light gray grid) more clearly showing the change of relative particle positions of the two layers, especially illustrated by the examples of the variations of the colored lattice lines labeled by *A1* to *A4* and *B1* to *B4* in layers *A* and *B*, respectively. The different ICMs in different regions of layers *A* and *B* shown in (a) are the key causing intra- and interlayer slips and 3D SRs.

fcc, bcc, and hcp 3D structures [27,42,46]. However, this effect decreases with decreasing particle diameter [27]. Without addressing dynamics as our work, layering from the system boundary with similar 2D intralayer and 3D structures to ours was also reported in the previous investigations on the dusty plasma system, even using larger dust particles 3.3 micrometer in diameter [27], and in the confined colloidal systems with isotropic Yukawa type interaction between two flat hard walls but without ion flow and gravity [26]. They demonstrate that ion flow effect is negligible on extending our findings to general confined Yukawa systems [42].

In conclusion, we have demonstrated the formation of surface induced layering with a fluctuating layering-liquid interface, and constructed a clear microscopic dynamical picture for the cooperative intralayer motion and induced structural rearrangement of the heterogeneous 3D structures, in a quenched 3D dusty plasma liquid suspended above a flat sheath boundary. It is found that, after quenching from a liquid with 2 to 3 layers adjacent to the bottom flat boundary, the layering front exponentially invades upward, and exhibits turbulentlike spatiotemporal fluctuations with power spectra following scale-free power law decays after reaching the steady state. The layered region can be viewed as a $2 + 1D$ system, with vertically coupled layers exhibiting hexatic intralayer structure composed of a small fraction of dislocations immersed in the triangular lattice background with long-range orientational order. The similar orientations but with different horizontal shifts of the intralayer lattice lines of adjacent layers allow the formation of 3D fcc, bcc, and hcp structures, only with [111], [110], and [001] lattice orientations normal to layers, respectively. The stick-slip ICMs are different for adjacent layers. It is the key for interlayer slip and leading to heterogeneous 3D structures and structural rearrangements. The averaged long-range intralayer lattice orientations can still be sustained over a long time due to the interlayer coupling.

This work is supported by the Ministry of Science and Technology, Taiwan, under Contract No. MOST-108-2112-M-008-015.

[1] F. H. Stillinger, *J. Chem. Phys.* **89**, 6461 (1988).
 [2] W. T. Juan and I. Lin, *Phys. Rev. Lett.* **80**, 3073 (1998); Y. J. Lai and L. I, *Phys. Rev. Lett.* **89**, 155002 (2002).
 [3] T. Kawasaki, T. Araki, and H. Tanaka, *Phys. Rev. Lett.* **99**, 215701 (2007).
 [4] K. Watanabe and H. Tanaka, *Phys. Rev. Lett.* **100**, 158002 (2008).
 [5] Y. Han, N. Y. Ha, A. M. Alsayed, and A. G. Yodh, *Phys. Rev. E* **77**, 041406 (2008).
 [6] L. Assoud, F. Ebert, P. Keim, R. Messina, G. Maret, and H. Löwen, *Phys. Rev. Lett.* **102**, 238301 (2009).
 [7] Z. Zhang, P. J. Yunker, P. Habdas, and A. G. Yodh, *Phys. Rev. Lett.* **107**, 208303 (2011).

[8] S. Deutschlander, T. Horn, H. Löwen, G. Maret, and P. Keim, *Phys. Rev. Lett.* **111**, 098301 (2013).
 [9] Y. S. Su, C. W. Io, and L. I, *Phys. Rev. E* **86**, 016405 (2012).
 [10] C. Yang, C. W. Io, and L. I, *Phys. Rev. Lett.* **109**, 225003 (2012).
 [11] A. L. Thorneywork, J. L. Abbott, D. G. A. L. Aarts, and R. P. A. Dullens, *Phys. Rev. Lett.* **118**, 158001 (2017).
 [12] C. L. Rhykerd, Jr., M. Schoen, D. J. Diestler, and J. H. Cushman, *Nature (London)* **330**, 461 (1987).
 [13] S. Granick, *Phys. Today* **52**, No. 7, 26 (1999).
 [14] M. Heuberger, M. Zach, and N. D. Spencer, *Science* **292**, 905 (2001).
 [15] P. A. Thompson, G. S. Grest, and M. O. Robbins, *Phys. Rev. Lett.* **68**, 3448 (1992).
 [16] B. Bhushan, J. N. Israelachvili, and U. Landman, *Nature (London)* **374**, 607 (1995).
 [17] J. Klein and E. Kumacheva, *Science* **269**, 816 (1995).
 [18] J. Gao, W. D. Luedtke, and U. Landman, *Phys. Rev. Lett.* **79**, 705 (1997).
 [19] L. W. Teng, P. S. Tu, and L. I, *Phys. Rev. Lett.* **90**, 245004 (2003).
 [20] R. Haghgoie and Patrick S. Doyle, *Phys. Rev. E* **72**, 011405 (2005).
 [21] C. W. Io and L. I, *Phys. Rev. E* **80**, 036401 (2009).
 [22] Q. L. Bi, Y. J. Lu, and W. H. Wang, *Phys. Rev. Lett.* **120**, 155501 (2018).
 [23] L. Chen, C. R. Cao, J. A. Shi, Z. Lu, Y. T. Sun, P. Luo, L. Gu, H. Y. Bai, M. X. Pan, and W. H. Wang, *Phys. Rev. Lett.* **118**, 016101 (2017).
 [24] D. G. Grier and C. A. Murray, *J. Chem. Phys.* **100**, 9088 (1994).
 [25] K. Sandomirski, E. Allahyarov, H. Löwen, and S. U. Egelhaaf, *Soft Matter* **7**, 8050 (2011).
 [26] S. Arai and H. Tanaka, *Nat. Phys.* **13**, 503 (2017).
 [27] M. Zuzic, A. V. Ivlev, J. Goree, G. E. Morfill, H. M. Thomas, H. Rothermel, U. Konopka, R. Sutterlin, and D. D. Goldbeck, *Phys. Rev. Lett.* **85**, 4064 (2000).
 [28] C. W. Io and L. I, *Phys. Rev. E* **85**, 026407 (2012).
 [29] C. Yang, W. Wang and L. I, *Phys. Rev. E* **93**, 013202 (2016).
 [30] V. Nosenko, J. Goree, and A. Piel, *Phys. Rev. Lett.* **97**, 115001 (2006).
 [31] C. A. Knapek, D. Samsonov, S. Zhdanov, U. Konopka, and G. E. Morfill, *Phys. Rev. Lett.* **98**, 015004 (2007).
 [32] Y. Feng, J. Goree, and B. Liu, *Phys. Rev. Lett.* **100**, 205007 (2008).
 [33] G. E. Morfill and A. V. Ivlev, *Rev. Mod. Phys.* **81**, 1353 (2009).
 [34] J. Goree, Z. Donkò, and P. Hartmann, *Phys. Rev. E* **85**, 066401 (2012).
 [35] A. Piel, D. Block, A. Melzer, M. Mulsow, J. Schablinski, A. Schella, F. Wieben, and J. Wilms, *Eur. Phys. J. D.* **72**, 80 (2018).
 [36] L. Couëdel, V. Nosenko, M. Rubin-Zuzic, S. Zhdanov, Y. Elskens, T. Hall, and A. V. Ivlev, *Phys. Rev. E* **97**, 043206 (2018).
 [37] N. P. Kryuchkov, E. V. Yakovlev, E. A. Gorbunov, L. Couëdel, A. M. Lipaev, and S. O. Yurchenko, *Phys. Rev. Lett.* **121**, 075003 (2018).

- [38] S. A. Khrapak, B. A. Klumov, P. Huber, V. I. Molotkov, A. M. Lipaev, V. N. Naumkin, H. M. Thomas, A. V. Ivlev, G. E. Morfill, O. F. Petrov, V. E. Fortov, Yu. Malentschenko, and S. Volkov, *Phys. Rev. Lett.* **106**, 205001 (2011).
- [39] S. A. Khrapak, B. A. Klumov, P. Huber, V. I. Molotkov, A. M. Lipaev, V. N. Naumkin, A. V. Ivlev, H. M. Thomas, M. Schwabe, G. E. Morfill, O. F. Petrov, V. E. Fortov, Yu. Malentschenko, and S. Volkov, *Phys. Rev. E* **85**, 066407 (2012).
- [40] B. Steinmuller, C. Dietz, M. Kretschmer, and M. H. Thoma, *Phys. Rev. E* **97**, 053202 (2018).
- [41] C. Dietz, R. Bergert, B. Steinmüller, M. Kretschmer, S. Mitic, and M. H. Thoma, *Phys. Rev. E* **97**, 043203 (2018).
- [42] See Supplemental Material at <http://link.aps.org/supplemental/10.1103/PhysRevLett.124.165001>, which includes Refs. [9,19,23–27,43–46], for more details about (a) the experimental method and the method to determine 3D microstructure, (b) the fluctuating front and front roughness, (c) heterogeneous intralayer motions of layers *A*, *B*, and *C* with a larger view, (d) mean square relative displacements of intra- and interlayer adjacent particles, (e) the ratio of the probability of interlayer (vertical) hopping to that of intralayer hopping, (f) the negligible ion focusing effect on inducing anisotropic particle interaction, and (g) the topological origin for layering from the confinement boundary.
- [43] D. Samsonov, A. Elsaesser, A. Edwards, H. M. Thomas, and G. E. Morfill, *Rev. Sci. Instrum.* **79**, 035102 (2008).
- [44] A. J. Allstadt, J. A. Newman, J. A. Walter, G. Korniss, and T. Caraco, *Sci. Rep.* **6**, 29908 (2016).
- [45] M. R. Zuzic, G. E. Morfill, A. V. Ivlev, R. Pompl, B. A. Klumov, W. Bunk, H. M. Thomas, H. Rothermel, O. Havnes, and A. Fouquet, *Nat. Phys.* **2**, 181 (2006).
- [46] V. A. Schweigert, I. V. Schweigert, A. Melzer, A. Homann, and A. Piel, *Phys. Rev. E* **54**, 4155 (1996).
- [47] Local bond orientational order for a 2D system is defined as $\Psi_6(\mathbf{r}) = 1/N \sum_k \exp(i6\theta_k)$, where θ_k and N are the bond angle from the dust at \mathbf{r} to its nearest neighbor k and the number of nearest neighbors, respectively. $|\Psi_6| = 1$ and < 0.4 for a perfect triangular lattice site and a defect site, respectively.
- [48] K. J. Strandburg, *Bond-Orientational Order in condensed Matter Systems* (Springer, New York, 1992).